Extending the Near-Infrared Emission Range of Indium Phosphide Quantum Dots for Multiplexed *In Vivo* Imaging

Alexander M. Saeboe, Alexey Yu. Nikiforov, Reyhaneh Toufanian, Joshua C. Kays, Margaret Chern, J. Paolo Casas, Keyi Han, Andrei Piryatinski, Dennis Jones, and Allison M. Dennis*

Cite This: *Nano Lett.* 2021, 21, 3271–3279

Read Online

ACCESS | Metrics & More | Article Recommendations | Supporting Information

ABSTRACT: This report of the reddest emitting indium phosphide quantum dots (InP QDs) to date demonstrates tunable, near-infrared (NIR) photoluminescence (PL) as well as PL multiplexing in the first optical tissue window while avoiding toxic constituents. This synthesis overcomes the InP "growth bottleneck" and extends the emission peak of InP QDs deeper into the first optical tissue window using an inverted QD heterostructure, specifically ZnSe/InP/ZnS core/shell/shell nanoparticles. The QDs exhibit InP shell thickness-dependent tunable emission with peaks ranging from 515–845 nm. The high absorptivity of InP yields effective photoexcitation of the QDs with UV, visible, and NIR wavelengths. These nanoparticles extend the range of tunable direct-bandgap emission from InP-based nanostructures, effectively overcoming a synthetic barrier that has prevented InP-based QDs from reaching their full potential as NIR imaging agents. Multiplexed lymph node imaging in a mouse model demonstrates the potential of the NIR-emitting InP particles for *in vivo* imaging.

KEYWORDS: *cadmium-free quantum dots, inverted quantum dot, indium phosphide, quantum well, preclinical imaging*
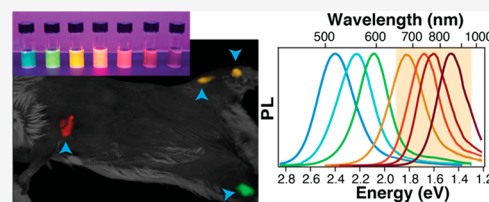
F luorescence is an important biomedical imaging modality because of the relatively low cost of imaging equipment, nominal toxicity of nonionizing radiation (i.e., light), potential for molecular imaging using target-specific contrast agents, and the prospect of multiplexed imaging using discretely colored fluorophores.[1,2] Molecules common in biological tissues including lipids, water, and hemoglobin both scatter and absorb light, limiting the ability of visible wavelengths to penetrate tissue structures.[3] However, tissue-penetrating fluorescence imaging is feasible in the first optical tissue window (650–950 nm), where both light scattering and absorption are reduced compared to visible wavelengths.[4] Semiconductor quantum dots (QDs) are inorganic nanoparticle emitters exhibiting size-dependent tunable emission peaks and broad, overlapping absorption peaks that are ideal for multiplexed imaging. While traditional cadmium selenide-based QDs are somewhat limited in their preclinical imaging applications because the CdSe bulk bandgap of 712 nm (1.74 eV) limits their emission range to visible wavelengths, the bandgap of indium phosphide at 925 nm (1.34 eV) promises tunability and multiplexing capacity throughout the NIR-I optical tissue window.[5,6] Cadmium-free QDs exhibit considerable promise for tissue-depth imaging both because of the advantages of the extended wavelength range and because of an interest in moving away from heavy metal-laden materials in the hopes of eliminating toxicity concerns.[7–11]

Recent advances in InP synthesis include the development of novel synthetic schemes that drive down the cost and environmental impact of InP synthesis while also improving photophysical performance.[12–15] These Type I and Quasi-Type II InP QDs exhibit high quantum yields with reasonably narrow emission peak full width half maximums (FWHM <40 nm),[15,16] but do not emit throughout the first optical tissue window; reported emission peaks for colloidal InP are all below 750 nm, regardless of synthesis method.[12,15–19] Indium phosphide cores with cadmium sulfide or cadmium selenide shells emit at wavelengths >1000 nm, but the Type II band alignment of these structures coincides with longer photoluminescence lifetimes and lower quantum yields in addition to the unfortunate inclusion of cadmium.[20–23] In order to address the shortcomings of InP tunability in the NIR, copper-doped InP and ternary systems such as copper indium sulfide have been developed.[24–26] These systems exhibit dopant-based NIR emission, but this emission mechanism is thought to inherently limit the maximum brightness of the emitters and increase the emission peak width.[24–29] Alternative NIR-emitting QD structures continue to be developed, including Ag_2S and Ag_2Se, which can exhibit narrow PL across the visible and NIR-II wavelength ranges.[30–32] However, despite intensive synthetic efforts, these silver-based systems suffer from comparably low quantum yields and poor photostability,
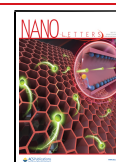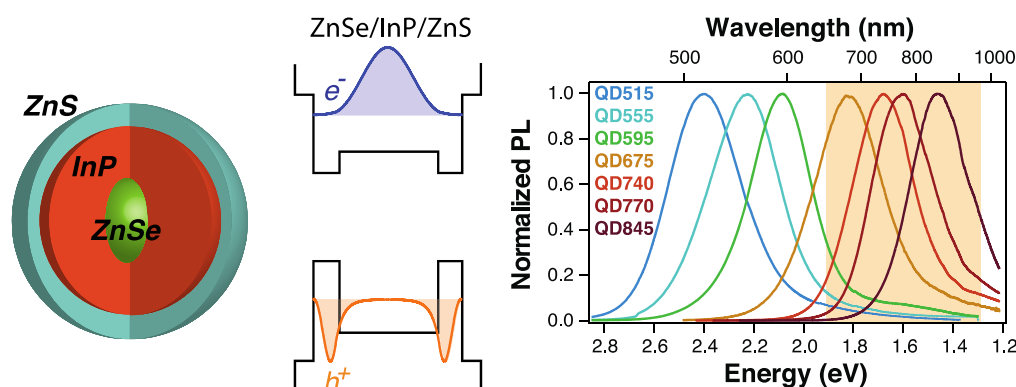
Figure 1. ZnSe/InP/ZnS core/shell/shell nanoparticles. The wide-bandgap ZnSe core acts as a spacer around which the optically active InP shell is wrapped. The resulting InP QDs can emit at longer wavelengths than existing literature reports of InP QDs and are tunable with shell thickness. From left to right: schematic of the core/shell/shell structure design, diagram of the ZnSe/InP/ZnS bandgap alignments with corresponding electron and hole wave functions, and normalized photoluminescence (PL) spectra of QDs with increasing InP deposition. Note the electron and hole densities presented are for a 3.4 nm ZnSe core with a 0.75 nm InP shell; the ZnS capping shell was modeled as an infinite well.

particularly at NIR wavelengths, even when shelled with wide bandgap semiconductors.[31−35] Our recent work describing CdSe shell emission demonstrated that lower energy/longer wavelength peak emission was feasible with confinement in the QD shell layer than with the same volume of CdSe in the traditional spherical QD morphology.[22,23] Given concerns that a "growth bottleneck" precludes synthesis of InP cores large enough to produce emission peaks spanning the entire NIR emission range theoretically possible for this material,[36] we hypothesized that an InP shell structure may enable lower energy emission than we have observed with InP cores.

In traditional Type I QDs, both the electron and hole reside in the semiconductor core, the size and composition of which dictates emission energy/wavelength/color. In Quasi-Type-II heterostructures, one charge carrier (electron or hole) is confined, but band offsets in either the conduction or valence band are close enough in energy that the excited electron or hole is delocalized.[6] In the prototypical case, that is, CdSe/CdS, the electron wave function spreads from the core into the shell material, while the wave function of the heavy hole is confined to the core.[37] In an Inverse-Type I semiconductor nanoparticle, a high bandgap core material is coated with a second semiconductor with a smaller bandgap and lower energy valence and conduction bands, confining the excited electron and the hole in the shell.[6] Cadmium-based Inverse-Type I structures were briefly mentioned in the QD literature over 10 years ago[38−40] but yielded minimal subsequent interest until recently.[41] A brief, singular report of thin-shelled, visible emitting ZnSe/InP/ZnS particles described them as Inverse-Type I structures.[42] We synthesized the inverted structure with concerted methods promoting the deposition of thick, epitaxial semiconductor shells[43−45] to generate cadmium-free NIR emission that pushes to longer wavelengths than reported thus far with Type I or Quasi-Type II InP core structures (Figure 1, Figure S1). These results highlight the advantages of nonconventional heterostructured QDs, while opening the door to further development of NIR-emitting InP nanoparticles.

The electronic structure of ZnSe/InP was calculated using a two-band effective mass model; the effect of the high bandgap ZnS cap (second shell) is negligible and was not accounted for in the calculations. The specific parameters used in the calculation are outlined in the SI. The result of the modeling shows that ZnSe/InP heterostructures with sufficiently thick

InP shells are predicted to exhibit Inverted-Type I electron and hole localization to the shell (Figure S2), while particles with less than 3 nm thick InP shells, like those demonstrated previously,[42] exhibit quasi-Type II band structure with the electron delocalized over the core and shell and the hole localized to the shell (see band diagram in Figure 1, Figure S3). In either case, the "heavy hole" of InP localizes to the InP shell as soon as it is >0.5 nm thick. This model predicts that the emission color of the ZnSe/InP structure can be tuned by changing the InP shell thickness, as has also been seen with ZnSe/CdSe inverted QDs.[46] ZnSe/CdSe inverted Type-I QDs exhibit Quasi Type-II/Type II behavior at intermediate shell thicknesses, but the electron localizes to the shell prior to the hole due to different CdSe and InP band offsets relative to the ZnSe cores. For both the ZnSe/InP and ZnSe/CdSe core/shells, Inverted Type-I band structure is predicted for thick-shelled heterostructures as both the electron and hole localize to the shell.[46] The bandgaps predicted by EMM indicate that both traditional[22,23] and inverted InP QD structures are theoretically capable of producing tunable emission through-out the first optical tissue window, but synthetic experience indicates that this has been technically challenging to achieve for InP core-based QDs, as these NIR emissions are not reported in the literature.

Inverted InP-based heterostructure reactions proceeded using hot-injection colloidal chemistry methods. First, zinc selenide cores were formed in a high-temperature, inert atmosphere precipitation reaction between zinc oleate and selenium complexed by diphenyl phosphine (Se/DPP), similar to previous reports.[47] The resulting ZnSe cores exhibit a clear 1S absorption peak, indicating quantum confinement and reasonably narrow size distribution (Figure S4). The ZnSe cores were purified in a glovebox under argon via ethanol precipitation and then resuspended in octadecene (ODE) with 10% (v/v) oleylamine (OAm). Under argon atmosphere on a Schlenk line, indium and phosphorus precursors were added via a modified successive ionic layer adsorption and reaction (SILAR) approach.[48] In a typical SILAR reaction, shell layers are added one ionic layer at a time through dropwise addition of the precursors followed by a high-temperature anneal (178 °C; 1 or 2.5 h) to ensure epitaxial crystal growth and reduce nucleation of the shell material. Although the ZnSe cores are zinc-terminated,[49] indicating that starting the SILAR reaction with the anionic phosphorus precursor should be preferred, we

found that starting with the anion led to nucleation of new InP QDs as SILAR progressed (data not shown). In contrast, we observed no evidence of nucleation when initiating SILAR with the indium cation, and we did observe spectral shifts in the ZnSe core absorbance after the addition of the first indium layer, indicating that the indium was binding to the ZnSe surface even in the absence of phosphorus, perhaps by displacing surface zinc atoms (data not shown). The indium and phosphorus precursors were 0.2 M indium oleate (1:3.3 In/oleic acid (OA)) in ODE and 0.2 M tris(trimethylsilyl)-phosphine ((TMS)$_3$P) in ODE, respectively. InP is highly susceptible to oxidation and these surface defects inhibit photoluminescence from the InP nanostructure,[50] so a second protective shell of zinc sulfide was added via SILAR using zinc oleate (0.2 M 1:3.3 Zn/OA) and 0.2 M sulfur dissolved in ODE to produce strongly emissive and chemically stable particles. The quantum yield (QY) of as-synthesized particles was sometimes further increased using a postsynthesis treatment process whereby cleaned particles were heated to 240 °C for 3 h with 0.2 M zinc oleate in trioctylphosphine (TOP), producing zinc-terminated particles.

Up to 16 rounds of SILAR were used to deposit the InP immediately followed by 2−3 rounds of ZnS SILAR. As can be seen with bright-field (BF) scanning transmission electron microscopy (STEM), the QDs gradually increase in size, indicating progressive growth of the InP layer with additional SILAR iterations (Figure 2a, Figures S5 and S6). Microwave plasma atomic emission spectroscopy (MP-AES; Agilent 4200MP-AES) of acid-digested samples yields the elemental composition of the core/shell/shell structures. Atomic concentrations in ppb were converted to molarity to calculate the relative abundance of the discrete elements for each sample. By combining the elemental ratios with the average particle size from STEM images and the assumption that the particles are concentric spheres comprising ZnSe/InP/ZnS, we estimated the relative core and shell dimensions for the QDs (Figure 2b). We assume that the relative volumes of the ZnSe core, InP shell, and ZnS shell are proportional to the molar ratios of Se, In, and Zn-minus-Se, respectively, adjusted for the crystal densities of each of the semiconductors. These results show that the InP shell grows progressively with an increased number of InP SILAR shelling iterations (Figure 2b, Table 1). The ZnS capping shell is ∼1 monolayer thick for each of the measured samples, consistent with the subquantitative reaction efficiency often seen with the Zn(OA)$_2$-based shelling protocol.

Precursor deposition and nanocrystal growth is also seen in the X-ray diffractograms of the materials (Figure 2c). The primary low-angle diffraction peak of sample QD515, observed at 28.2°, is at a considerably higher angle than the ZnSe core peak, observed at 27.2°, and close to the ZnS peak position 28.5°. This shift toward a characteristic ZnS X-ray diffraction pattern suggests that the QD515 sample volume is dominated by ZnS. In contrast, samples QD675 and QD740, with primary low angle diffraction peaks at 26.6° and 26.5°, respectively, approach the characteristic InP diffraction peak at 26.3°, indicating that these QDs largely comprise InP by volume. These sample diffraction peak shifts are consistent with the elemental volume predominance expected. Samples with few InP SILAR cycles exhibit a substantial ZnS contribution to the XRD diffractogram, while the predominance of the InP peaks increases with larger numbers of InP SILAR cycles. Nanocrystal growth is also clearly observed based on a narrowing of
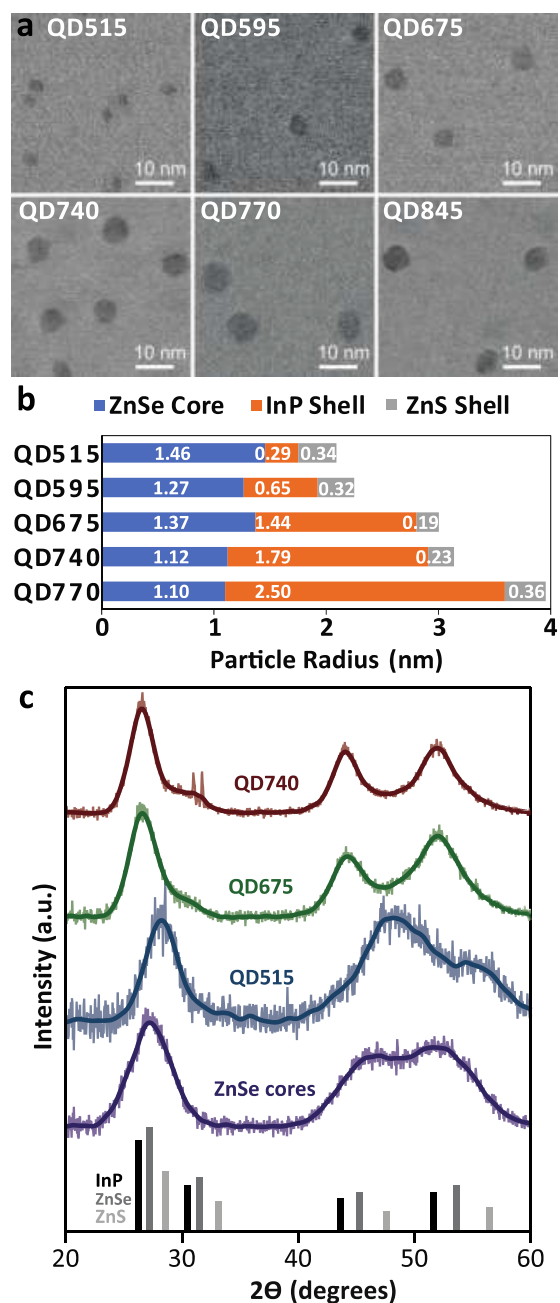

Figure 2. Materials characterization of QDs. (a) Bright-field (BF) STEM images of samples QD515, QD595, QD675, QD740, QD770, and QD845. (b) ZnSe/InP/ZnS core/shell/shell dimensions based on atomic analysis (MP-AES), assuming concentric spheres with total diameter equal to the average diameter determined by STEM. The sample is indicated on the left with the component dimension noted in nm on the bar section corresponding to the ZnSe radius (blue), InP shell (orange), and ZnS shell (gray). (c) X-ray diffractograms (XRD) of the ZnSe cores and several QDs, along with vertical lines representing reference InP, ZnSe, and ZnS peaks from the Crystallography Open Database (COD).

the XRD peaks for samples with larger numbers of InP SILAR cycles. This narrowing is particularly evident in the 40−60° range: the two characteristic zincblende diffraction peaks of the ZnSe cores and QD515 in this region are sufficiently broad that the individual peaks are not readily resolvable, while samples QD675 and QD740 have two clearly resolvable peaks. Further growth of the nanocrystals is also supported by a

Table 1. Summary of QD Properties

sample name	sample description	diameter [nm][a]	InP shell thickness [nm/ML][b]	1S peak position [nm/eV][c]	PL peak (FWHM) [nm/eV]	Ave. PL lifetime, $\bar{\tau}$ [ns][d]
ZnSe	ZnSe core	2.0		356 nm	369 (19) nm	
				3.48 eV	3.36 (0.18) eV	
QD515	ZnSe/2InP/3ZnS	4.2 ± 0.60 (14%)	0.29 nm	482 nm	517 (75) nm	69
			0.9 ML	2.57 eV	2.40 (0.35) eV	
QD555	ZnSe/3InP/3ZnS	4.3 ± 0.79 (18%)		520 nm	557 (84) nm	66
				2.38 eV	2.23 (0.34) eV	
QD595	ZnSe/4InP/3ZnS	4.5 ± 0.84 (19%)	0.91 nm	572 nm	595 (82) nm	50
			1.9 ML	2.17 eV	2.08 (0.29) eV	
QD675	ZnSe/7InP/2ZnS	6.0 ± 0.86 (14%)	1.44 nm	648 nm	677 (123) nm	91
			4.3 ML	1.91 eV	1.83 (0.33) eV	
QD740	ZnSe/10InP/2ZnS	6.3 ± 0.99 (16%)	1.79 nm	702 nm	738 (129)	75
			5.3 ML	1.77 eV	1.68 (0.29) eV	
QD770	ZnSe/13InP/3ZnS	7.9 ± 0.96 (12%)	2.50 nm	731 nm	771 (145) nm	85
			7.4 ML	1.70 eV	1.61 (0.30)	
QD845[e]	ZnSe/16InP/2ZnS	6.8 ± 0.71 (10%)		735 nm	845 (174) nm	132
				1.69 eV	1.47 (0.29) eV	

[a]ZnSe core diameter determined from 1S peak position.[49] Diameters of particles for samples QD515 and QD595−QD845 were determined from BF STEM dark-field images. Particle diameter for sample QD555 determined using TEM images. Error represents standard deviation of diameters for n = 129−240 measured particles. [b]InP shell thickness determined by combining STEM-based diameter measurements and elemental ratios of In, Se, and Zn determined by MP-AES. Not determined for QD555 and QD845 due to a lack of sample available for MP-AES elemental analysis. [c]As determined from the derivative of the absorbance spectrum.[12] [d]ZnSe cores emit out of the wavelength range measurable on our lifetime instrument. [e]All samples in this size series use the same 2.0 nm diameter ZnSe core except QD845, which was synthesized with 16 rounds of InP SILAR on a 3.1 nm diameter ZnSe core.

reduction in FWHM of the primary low-angle diffraction peak from 2.8° to 2.3° for QD675 to QD770, respectively. In addition to crystal size and composition, the XRD peak position and width could also be affected by strain effects; however, these strain effects are difficult to predict and therefore are not considered explicitly.[51,52]

The presence of constituent elements in QD clusters was examined using energy dispersive spectrometry (EDS) mapping using a Super-X EDS detector on Tecnai Osiris TEM operated in STEM mode (Figure 3). EDS elemental mapping was performed on the samples before and after deposition of the outer ZnS shell. Since the electron beam excites X-rays from both ZnSe core and its outer InP and ZnS shells, the elemental maps show a relative elemental distribution averaged over the entire particle volume probed. The elements present in the mapped dots include zinc and selenium from the cores and indium and phosphorus from the inner shells with sulfur detected at 2.3 keV after addition of the outer ZnS shell. Also appearing in the EDS spectra are the energy lines corresponding to copper from the grid with supporting carbon membrane.

The QDs exhibit InP deposition-dependent quantum confinement and optical properties (Figure 4). InP QDs grown on the same ZnSe cores emit redder with additional InP shell depositions. For example, the synthesis of QD515, QD555, QD595, QD675, QD740, and QD770 all used the same 2.0 nm diameter ZnSe core combined with 2, 3, 4, 7, 10, and 13 rounds of In and P SILAR addition, respectively, and 2−3 rounds of ZnS addition. The InP shelling reaction was repeated with subtle changes to the reaction conditions on different batches of ZnSe cores, yielding similar tunability with InP addition (Figure S7, Table S1). Of these samples, only QD845, which was synthesized with 16 rounds of SILAR on a 3.1 nm diameter ZnSe core, is included together with the primary series to avoid redundancy.

The InP from additional rounds of SILAR deposition enhance the concentration-normalized absorbance of the particles (Figure 4a, Figure S8), as is appropriate given the larger volume of InP per particle. The distinct 1S peaks seen in the photoluminescence excitation (PLE) spectra of the InP QDs emitting in the visible wavelength regime (Figure 4b) are indicative of quantum confinement. The QD samples exhibited absolute quantum yields up to 38%, as measured in an integrating sphere (Horiba Quanta-ϕ) (Table S2). For the three reddest emitters, which exhibited significant PL outside the calibrated range of our integrating sphere, we used the directly measured absolute QY and full PL spectrum to extrapolate the QY of the redder region using the relative area under the curve.

The weighted average photoluminescence lifetimes of the InP QDs, determined using a triexponential fit, are between 80 and 140 ns, similar to previously observed lifetimes seen for InP QDs (Figure 4c, Table 1, Table S3).[20,22,23,53,54] The inverted InP QD emission peaks are broad compared to InP core-based systems however, and the largest particles exhibit red-tail emission >1000 nm, which is beyond the bulk bandgap of InP. Investigation of the fluorescent lifetimes of different spectral regions of the QD555 and QD675 emission peaks (i.e., blue tail, peak, and red tail emission) reveal wavelength region-dependent differences in the fluorescent lifetimes, as shown in Figure S9. Specifically, the weighted average PL lifetimes increase with increasing emission wavelength (i.e., $\bar{\tau}_{\text{blue tail}} < \bar{\tau}_{\text{peak}} < \bar{\tau}_{\text{red}}$ tail). This trend is particularly evident for the transition from the emission spectra peak region to the red tail, where the average lifetimes increase from 102 to 223 ns and 147 to 426 ns for QD555 and QD675, respectively (Table S4). The breadth of the emission peak and differences in the lifetimes suggest that there may be different emission mechanisms between these spectral regions of the inverted QD system or, alternatively, a heterogeneous particle population. While there is precedent for QD systems with
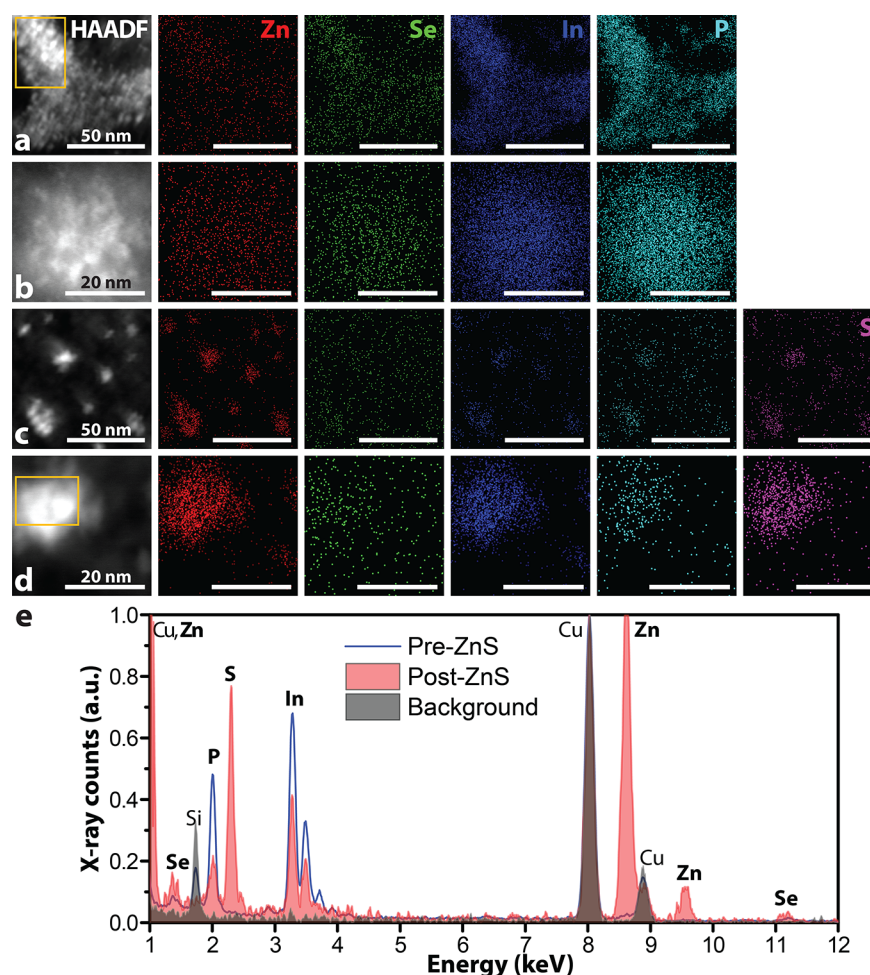
Figure 3. Elemental dispersive X-ray spectroscopy (EDS). Elemental maps showing the distribution of each element of interest alongside a reference high-angle annular dark field (HAADF) image indicating the spatial position of particle clusters; scale bars in the elemental maps are the same as the corresponding HAADF image. QD515 (a,b) before and (c,d) after ZnS capping. To generate the elemental maps, the X-ray K lines were used for Zn, P, and S, while X-ray L lines were used for In and Se. (e) EDS spectra collected from yellow inset regions in the reference HAADF images show the presence of elements in a cluster of QD. A representative background spectrum is included for reference; spectral intensities are normalized to the copper peak at 8 keV.

more than one emission mechanism,[55,56] further studies will be required to ascertain the precise source of the wavelength dependent lifetimes in this QD system.

Notably, the NIR-emitting particles exhibit significant absorption and PLE > 600 nm (Figure 4). Efficient excitation with red and NIR light ensures that penetrating wavelengths can be used for *in vivo* photoluminescence, enhancing the usefulness for preclinical imaging. Through this inverted InP QD synthesis, we have achieved extended emission tunability compared to what has been previously published for InP core-based QDs, yielding multiple emitters in the first optical tissue window. In order to generate bright NIR emitters for *in vivo* imaging of sentinel lymph nodes, QD675, QD770, and QD845 were Zn-TOP treated to enhance their brightness. As a result of this treatment, the QY of the QDs increased, but the emission peaks of the two longer wavelength emitters blue-shifted to QD720 and QD790, respectively (Table S2). Following a previously published protocol, QDs were rendered water-soluble through encapsulation in lipid-PEG micelles using 1,2-distearoyl-sn-glycero-3-phosphoethanolamine-*N*-[methoxy(polyethylene glycol)] (ammonium salt) with 5000 Da PEG (DSPE-PEG5k, Avanti Polar Lipids, Inc.).[57,58] The water-soluble samples largely retained their precoating bright-

ness, exhibiting QYs between 11 and 18%, consistent with similarly treated commercial QD705s (Thermo Fisher) (Table S2).

To demonstrate multiplexed *in vivo* imaging with the NIR-emitting InP QDs, the three Zn-TOP-treated samples were encapsulated in in DSPE-PEG5K, buffer exchanged into phosphate buffered saline (PBS), and sterile filtered. QDs were subcutaneously injected into a BALB/cJ mouse in three distinct sites to visualize lymphatic drainage. QD675 and QD790 were injected into the right and left hock, respectively. QD720 was injected into the right second mammary fat pad (Figure 5a). The mouse was imaged using an In Vivo Imaging System (IVIS Spectrum; PerkinElmer) at several time points post injection (p.i.), and the resulting images were analyzed and unmixed using the Living Image software (PerkinElmer) to show the emission from each QD. At 28 min p.i., drainage from the initial site of injection to local lymph nodes (LNs) was observed for all three of the QDs (Figure 5b). One hour p.i., lymphatic drainage is visible in the collecting lymphatic vessel extending from the left inguinal LN to the left axillary LN (Figure 5c). We included an inset at higher thresholding that shows the inguinal LN itself, since the low thresholding that enables visualization of the lymphatic drainage vessel
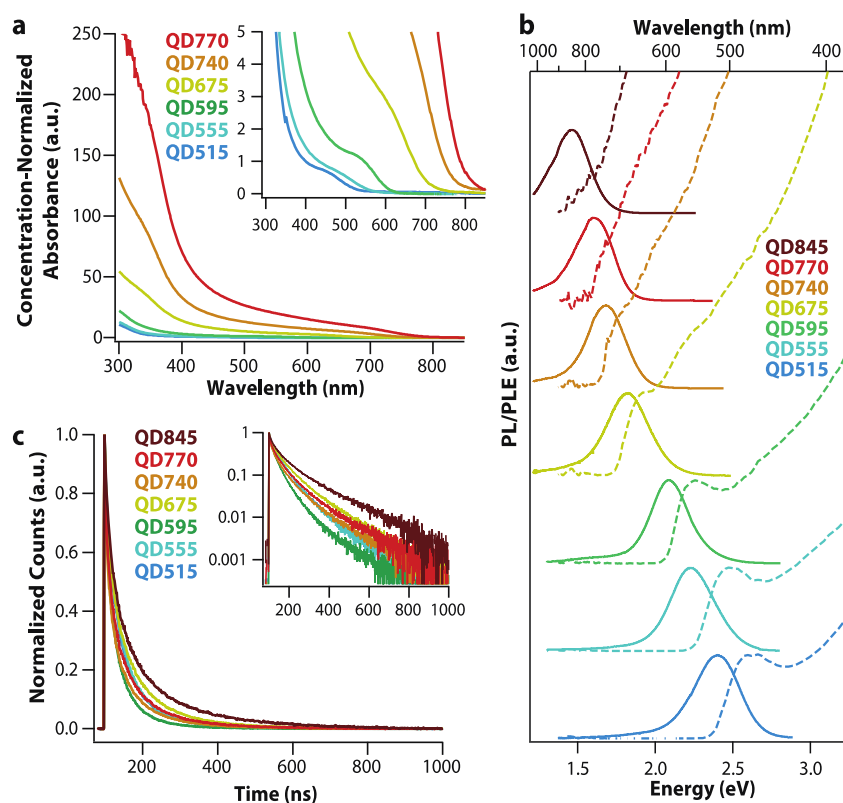
Figure 4. Optical properties of QDs. (a) Concentration-normalized absorbance was determined by measuring the absorption of carefully diluted reaction products (unwashed) from reactions loaded with identical amounts of the same ZnSe core and adjusted for reactant addition volumes. (b) Normalized photoluminescence and photoluminescence excitation spectra. (c) Photoluminescence lifetime following excitation at 405 nm.
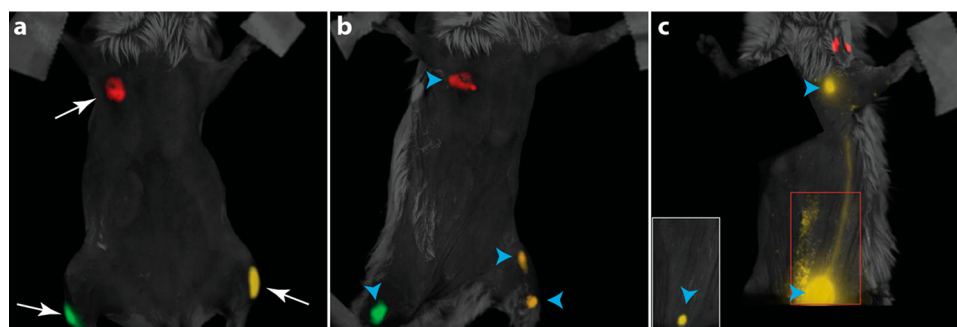

Figure 5. Spectrally unmixed images of a BALB/cJ mouse injected with three distinct QD solutions: QD675 (green; left hock injection), QD790 (gold; right hock injection), and QD720 (red, left armpit). (a) Injection sites imaged immediately post injection (p.i.). (b) Localization of QD675 in the left inguinal lymph node (LN), QD720 in the axillary LN, and QD790 in the right inguinal LN and popliteal LN 48 min p.i. (c) Lateral image 1 h p.i. shows QD790 lymphatic drainage from the inguinal LN to the axillary LN; inset of the boxed region with higher thresholding shows the contrast localized in the inguinal LN without image saturation. Images taken on PerkinElmer IVIS Spectrum and analyzed using Living Image software. White arrows indicate injection sites, while blue arrowheads indicate LNs.

causes saturation of the region (Figure 5, Figure S10). Visualization of QD720 and QD790 in the lymph nodes was possible at up to 52 h p.i. when the animal was sacrificed, and the body cavity exposed to confirm the colocalization of QDs with LNs (Figure S11). QD720 and QD790 were located in the axillary LNs on their respective sides of injection. QD790 was also seen in several LNs near the inguinal node as well as the inguinal LN itself. QD675 was not detected during the post-mortem analysis.

In summary, through multicomponent InP SILAR deposition in the presence of ZnSe cores, we synthesized indium phosphide-based QDs that exceed the previous NIR emission limits for this important cadmium-free composition. These small, bright nanocrystals comprising only In, P, Zn, S, and Se can be tuned to emit throughout the first optical tissue window, presenting an opportunity for multiplexed fluorescent imaging in the NIR, with QYs consistent with commercially available cadmium-based QDs. Subsequent work will optimize the synthesis to narrow the emission bandwidths, further improve brightness, and tailor the colloidal coating for targeted imaging.

■ ASSOCIATED CONTENT

Ⓢ Supporting Information

The Supporting Information is available free of charge at https://pubs.acs.org/doi/10.1021/acs.nanolett.1c00600.

A full description of the nanoparticle synthesis and coating procedure as well as additional characterization results are included in the Supporting Information (PDF).

■ AUTHOR INFORMATION

Corresponding Author

Allison M. Dennis − *Division of Materials Science and Engineering, Photonics Center, and Department of Biomedical Engineering, Boston University, Boston, Massachusetts 02215, United States;* ⓞ orcid.org/0000-0001-5759-9905; Email: aldennis@bu.edu

Authors

Alexander M. Saeboe − *Division of Materials Science and Engineering, Boston University, Boston, Massachusetts 02215, United States*

Alexey Yu. Nikiforov − *Photonics Center, Boston University, Boston, Massachusetts 02215, United States*

Reyhaneh Toufanian − *Division of Materials Science and Engineering, Boston University, Boston, Massachusetts 02215, United States*

Joshua C. Kays − *Department of Biomedical Engineering, Boston University, Boston, Massachusetts 02215, United States*

Margaret Chern − *Division of Materials Science and Engineering, Boston University, Boston, Massachusetts 02215, United States;* ⓞ orcid.org/0000-0003-3993-5500

J. Paolo Casas − *Department of Biomedical Engineering, Boston University, Boston, Massachusetts 02215, United States*

Keyi Han − *Department of Biomedical Engineering, Boston University, Boston, Massachusetts 02215, United States*

Andrei Piryatinski − *Theoretical Division, Los Alamos National Laboratory, Los Alamos, New Mexico 87544, United States*

Dennis Jones − *School of Medicine, Boston University, Boston, Massachusetts 02118, United States*

Complete contact information is available at:
https://pubs.acs.org/10.1021/acs.nanolett.1c00600

Author Contributions

A.M.S and A.M.D. conceived of the project. A.M.S., A.Yu.N., R.T., J.C.K., M.C., and A.M.D. designed experiments. A.M.S. performed the synthesis and micelle encapsulation of QDs, as well as MP-AES experiments. A.Yu.N. and A.M.S. carried out STEM and EDS experiments. A.M.S., J.C.K., and R.T. performed optical analysis. J.P.C. and K.H. performed STEM sizing. A.M.S. and D.J. performed the lymph node imaging experiments. A.P. performed EMM calculations. A.M.S. and A.M.D. wrote the manuscript with comments and editing from coauthors, and all authors have given approval to the final version of the manuscript.

Notes

The authors declare no competing financial interest.

■ ACKNOWLEDGMENTS

■ REFERENCES

(1) Hong, G.; Antaris, A. L.; Dai, H. Near-infrared fluorophores for biomedical imaging. *Nature Biomedical Engineering* **2017**, *1* (1), 1−22.

(2) Yun, S. H.; Kwok, S. J. J. Light in diagnosis, therapy and surgery. *Nature Biomedical Engineering* **2017**, *1* (1), 1−16.

(3) Jacques, S. L. Optical properties of biological tissues: a review. *Phys. Med. Biol.* **2013**, *58* (11), R37−R61.

(4) Smith, A. M.; Mancini, M. C.; Nie, S. M. Bioimaging Second Window for in Vivo Imaging. *Nat. Nanotechnol.* **2009**, *4* (11), 710−711.

(5) Aswathy, R. G.; Yoshida, Y.; Maekawa, T.; Kumar, D. S. Near-infrared quantum dots for deep tissue imaging. *Anal. Bioanal. Chem.* **2010**, *397* (4), 1417−1435.

(6) Reiss, P.; Protière, M.; Li, L. Core/shell semiconductor nanocrystals. *Small* **2009**, *5* (2), 154−168.

(7) Cassette, E.; Helle, M.; Bezdetnaya, L.; Marchal, F.; Dubertret, B.; Pons, T. Design of new quantum dot materials for deep tissue infrared imaging. *Adv. Drug Delivery Rev.* **2013**, *65* (5), 719−731.

(8) Xu, G.; Zeng, S.; Zhang, B.; Swihart, M.; Yong, K.; Prasad, P. New Generation Cadmium-Free Quantum Dots for Biophotonics and Nanomedicine. *Chem. Rev.* **2016**, *116* (19), 12234−12327.

(9) Kays, J. C.; Saeboe, A. M.; Toufanian, R.; Kurant, D. E.; Dennis, A. M. Shell-Free Copper Indium Sulfide Quantum Dots Induce Toxicity in Vitro and in Vivo. *Nano Lett.* **2020**, *20* (3), 1980−1991.

(10) Atha, D. H.; Nagy, A.; Steinbruck, A.; Dennis, A. M.; Hollingsworth, J. A.; Dua, V.; Iyer, R.; Nelson, B. C. Quantifying engineered nanomaterial toxicity: comparison of common cytotoxicity and gene expression measurements. *J. Nanobiotechnol.* **2017**, *15* (1), 79.

(11) Reiss, P.; Carriere, M.; Lincheneau, C.; Vaure, L.; Tamang, S. Synthesis of Semiconductor Nanocrystals, Focusing on Nontoxic and Earth-Abundant Materials. *Chem. Rev.* **2016**, *116* (18), 10731−10819.

(12) Tessier, M.; Dupont, D.; De Nolf, K.; De Roo, J.; Hens, Z. Economic and Size-Tunable Synthesis of InP/ZnE (E = S, Se) Colloidal Quantum Dots. *Chem. Mater.* **2015**, *27* (13), 4893−4898.

(13) Buffard, A.; Dreyfuss, S.; Nadal, B.; Heuclin, H.; Xu, X.; Patriarche, G.; Mézailles, N.; Dubertret, B. Mechanistic Insight and Optimization of InP Nanocrystals Synthesized with Aminophosphines. *Chem. Mater.* **2016**, *28* (16), 5925−5934.

(14) Li, Y.; Hou, X.; Dai, X.; Yao, Z.; Lv, L.; Jin, Y.; Peng, X. Stoichiometry-Controlled InP-Based Quantum Dots: Synthesis, Photoluminescence, and Electroluminescence. *J. Am. Chem. Soc.* **2019**, *141* (16), 6448−6452.

(15) Won, Y.-H.; Cho, O.; Kim, T.; Chung, D.-Y.; Kim, T.; Chung, H.; Jang, H.; Lee, J.; Kim, D.; Jang, E. Highly efficient and stable InP/

ZnSe/ZnS quantum dot light-emitting diodes. *Nature* **2019**, *575* (7784), 634−638.

(16) Ramasamy, P.; Kim, N.; Kang, Y.-S.; Ramirez, O.; Lee, J.-S. Tunable, Bright, and Narrow-Band Luminescence from Colloidal Indium Phosphide Quantum Dots. *Chem. Mater.* **2017**, *29* (16), 6893−6899.

(17) Xu, S.; Ziegler, J.; Nann, T. Rapid synthesis of highly luminescent InP and InP/ZnS nanocrystals. *J. Mater. Chem.* **2008**, *18* (23), 2653−2656.

(18) Xie, R.; Battaglia, D.; Peng, X. Colloidal InP nanocrystals as efficient emitters covering blue to near-infrared. *J. Am. Chem. Soc.* **2007**, *129* (50), 15432−15433.

(19) Reid, K.; McBride, J.; Freymeyer, N.; Thal, L.; Rosenthal, S. Chemical Structure, Ensemble and Single-Particle Spectroscopy of Thick-Shell InP-ZnSe Quantum Dots. *Nano Lett.* **2018**, *18* (2), 709−716.

(20) Dennis, A. M.; Mangum, B. D.; Piryatinski, A.; Park, Y.-S.; Hannah, D. C.; Casson, J. L.; Williams, D. J.; Schaller, R. D.; Htoon, H.; Hollingsworth, J. A. Suppressed Blinking and Auger Recombination in Near-Infrared Type-II InP/CdS Nanocrystal Quantum Dots. *Nano Lett.* **2012**, *12* (11), 5545−5551.

(21) Mangum, B. D.; Wang, F.; Dennis, A. M.; Gao, Y. Q.; Ma, X. D.; Hollingsworth, J. A.; Htoon, H. Competition between Auger Recombination and Hot-Carrier Trapping in PL Intensity Fluctuations of Type II Nanocrystals. *Small* **2014**, *10* (14), 2892−2901.

(22) Dennis, A. M.; Buck, M. R.; Wang, F.; Hartmann, N.; Majumder, S.; Casson, J.; Watt, J. D.; Doorn, S.; Htoon, H.; Sykora, M.; Hollingsworth, J. A. Role of Interface Chemistry in Opening New Radiative Pathways in InP/CdSe Giant Quantum Dots with Blinking-Suppressed Two-Color Emission. *Adv. Funct. Mater.* **2019**, *29* (37), 1809111.

(23) Toufanian, R.; Piryatinski, A.; Mahler, A. H.; Iyer, R.; Hollingsworth, J. A.; Dennis, A. M. Bandgap Engineering of Indium Phosphide-Based Core/Shell Heterostructures Through Shell Composition and Thickness. *Frontiers in Chemistry* **2018**, *6* (567), 12.

(24) Girma, W. M.; Fahmi, M. Z.; Permadi, A.; Abate, M. A.; Chang, J.-Y. Synthetic strategies and biomedical applications of I-III-VI ternary quantum dots. *J. Mater. Chem. B* **2017**, *5* (31), 6193−6216.

(25) Xie, R. G.; Peng, X. G. Synthesis of Cu-Doped InP Nanocrystals (d-dots) with ZnSe Diffusion Barrier as Efficient and Color-Tunable NIR Emitters. *J. Am. Chem. Soc.* **2009**, *131* (30), 10645−10651.

(26) Allen, P. M.; Bawendi, M. G. Ternary I-III-VI Quantum Dots Luminescent in the Red to Near-Infrared. *J. Am. Chem. Soc.* **2008**, *130* (29), 9240−9241.

(27) Bai, X.; Purcell-Milton, F.; Gun'ko, Y. K. Optical Properties, Synthesis, and Potential Applications of Cu-Based Ternary or Quaternary Anisotropic Quantum Dots, Polytypic Nanocrystals, and Core/Shell Heterostructures. *Nanomaterials* **2019**, *9* (1), 85.

(28) Liu, S.; Zhang, H.; Qiao, Y.; Su, X. One-pot synthesis of ternary CuInS2 quantum dots with near-infrared fluorescence in aqueous solution. *RSC Adv.* **2012**, *2* (3), 819−825.

(29) Cassette, E.; Pons, T.; Bouet, C.; Helle, M.; Bezdetnaya, L.; Marchal, F.; Dubertret, B. Synthesis and Characterization of Near-Infrared Cu-In-Se/ZnS Core/Shell Quantum Dots for In vivo Imaging. *Chem. Mater.* **2010**, *22* (22), 6117−6124.

(30) Lu, H.; Carroll, G. M.; Neale, N. R.; Beard, M. C. Infrared Quantum Dots: Progress, Challenges, and Opportunities. *ACS Nano* **2019**, *13* (2), 939−953.

(31) Tang, R.; Xue, J.; Xu, B.; Shen, D.; Sudlow, G. P.; Achilefu, S. Tunable Ultrasmall Visible-to-Extended Near-Infrared Emitting Silver Sulfide Quantum Dots for Integrin-Targeted Cancer Imaging. *ACS Nano* **2015**, *9* (1), 220−230.

(32) Lu, C.; Chen, G.; Yu, B.; Cong, H. Recent Advances of Low Biological Toxicity Ag2S QDs for Biomedical Application. *Adv. Eng. Mater.* **2018**, *20* (6), 1700940.

(33) Awasthi, P.; An, X.; Xiang, J.; Kalva, N.; Shen, Y.; Li, C. Facile synthesis of noncytotoxic PEGylated dendrimer encapsulated silver sulfide quantum dots for NIR-II biological imaging. *Nanoscale* **2020**, *12* (9), 5678−5684.

(34) Ovchinnikov, O. V.; Perepelitsa, A. S.; Smirnov, M. S.; Latyshev, A. N.; Grevtseva, I. G.; Vasiliev, R. B.; Goltsman, G. N.; Vitukhnovsky, A. G. Luminescence of colloidal Ag2S/ZnS core/shell quantum dots capped with thioglycolic acid. *J. Lumin.* **2020**, *220*, 117008.

(35) Song, J.; Ma, C.; Zhang, W.; Li, X.; Zhang, W.; Wu, R.; Cheng, X.; Ali, A.; Yang, M.; Zhu, L.; Xia, R.; Xu, X. Bandgap and Structure Engineering via Cation Exchange: From Binary Ag2S to Ternary AgInS2, Quaternary AgZnInS alloy and AgZnInS/ZnS Core/Shell Fluorescent Nanocrystals for Bioimaging. *ACS Appl. Mater. Interfaces* **2016**, *8* (37), 24826−24836.

(36) Li, Y.; Pu, C. D.; Peng, X. G. Surface activation of colloidal indium phosphide nanocrystals. *Nano Res.* **2017**, *10* (3), 941−958.

(37) Garcia-Santamaria, F.; Chen, Y.; Vela, J.; Schaller, R. D.; Hollingsworth, J. A.; Klimov, V. I. Suppressed Auger Recombination in "Giant" Nanocrystals Boosts Optical Gain Performance. *Nano Lett.* **2009**, *9* (10), 3482−3488.

(38) Battaglia, D.; Li, J. J.; Wang, Y. J.; Peng, X. G. Colloidal two-dimensional systems: CdSe quantum shells and wells. *Angew. Chem., Int. Ed.* **2003**, *42* (41), 5035−5039.

(39) Balet, L. P.; Ivanov, S. A.; Piryatinski, A.; Achermann, M.; Klimov, V. I. Inverted core/shell nanocrystals continuously tunable between type-I and type-II localization regimes. *Nano Lett.* **2004**, *4* (8), 1485−1488.

(40) Zhong, X. H.; Xie, R. G.; Zhang, Y.; Basche, T.; Knoll, W. High-quality violet- to red-emitting ZnSe/CdSe core/shell nanocrystals. *Chem. Mater.* **2005**, *17* (16), 4038−4042.

(41) Razgoniaeva, N.; Moroz, P.; Yang, M.; Budkina, D.; Eckard, H.; Augspurger, M.; Khon, D.; Tarnovsky, A.; Zamkov, M. One-Dimensional Carrier Confinement in "Giant" CdS/CdSe Excitonic Nanoshells. *J. Am. Chem. Soc.* **2017**, *139* (23), 7815−7822.

(42) Kim, S.; Park, J.; Kim, T.; Jang, E.; Jun, S.; Jang, H.; Kim, B.; Kim, S. W. Reverse Type-I ZnSe/InP/ZnS Core/Shell/Shell Nanocrystals: Cadmium-Free Quantum Dots for Visible Luminescence. *Small* **2011**, *7* (1), 70−73.

(43) Chen, Y.; Vela, J.; Htoon, H.; Casson, J. L.; Werder, D. J.; Bussian, D. A.; Klimov, V. I.; Hollingsworth, J. A. "Giant" multishell CdSe nanocrystal quantum dots with suppressed blinking. *J. Am. Chem. Soc.* **2008**, *130* (15), 5026−5027.

(44) Ghosh, Y.; Mangum, B. D.; Casson, J. L.; Williams, D. J.; Htoon, H.; Hollingsworth, J. A. New Insights into the Complexities of Shell Growth and the Strong Influence of Particle Volume in Nonblinking "Giant" Core/Shell Nanocrystal Quantum Dots. *J. Am. Chem. Soc.* **2012**, *134* (23), 9634−9643.

(45) Chern, M.; Nguyen, T. T.; Mahler, A. H.; Dennis, A. M. Shell thickness effects on quantum dot brightness and energy transfer. *Nanoscale* **2017**, *9* (42), 16446−16458.

(46) Cao, J.; Jiang, Z.-J. Thickness-dependent Shell Homogeneity of ZnSe/CdSe Core/Shell Nanocrystals and Their Spectroscopic and Electron- and Hole-transfer Dynamics Properties. *J. Phys. Chem. C* **2020**, *124* (22), 12049−12064.

(47) Yu, K.; Hrdina, A.; Zhang, X.; Ouyang, J.; Leek, D. M.; Wu, X.; Gong, M.; Wilkinson, D.; Li, C. Highly-photoluminescent ZnSe nanocrystals via a non-injection-based approach with precursor reactivity elevated by a secondary phosphine. *Chem. Commun.* **2011**, *47* (31), 8811−8813.

(48) Li, J. J.; Wang, Y. A.; Guo, W. Z.; Keay, J. C.; Mishima, T. D.; Johnson, M. B.; Peng, X. G. Large-scale synthesis of nearly monodisperse CdSe/CdS core/shell nanocrystals using air-stable reagents via successive ion layer adsorption and reaction. *J. Am. Chem. Soc.* **2003**, *125* (41), 12567−12575.

(49) Toufanian, R.; Zhong, X.; Kays, J.; Saeboe, A.; Dennis, A. ZnSe Quantum Dots: Determination of Molar Extinction Coefficient for UV to Blue Emitters. **2020**, *Chem Rxiv.* DOI: 10.26434/chemrxiv.13363706.v2 (accessed March 9, 2021).

(50) Jasinski, J.; Leppert, V. J.; Lam, S. T.; Gibson, G. A.; Nauka, K.; Yang, C. C.; Zhou, Z. L. Rapid oxidation of InP nanoparticles in air. *Solid State Commun.* **2007**, *141* (11), 624−627.

(51) Smith, A. M.; Mohs, A. M.; Nie, S. Tuning the optical and electronic properties of colloidal nanocrystals by lattice strain. *Nat. Nanotechnol.* **2009**, *4* (1), 56−63.

(52) Tschirner, N.; Lange, H.; Schliwa, A.; Biermann, A.; Thomsen, C.; Lambert, K.; Gomes, R.; Hens, Z. Interfacial Alloying in CdSe/CdS Heteronanocrystals: A Raman Spectroscopy Analysis. *Chem. Mater.* **2012**, *24* (2), 311−318.

(53) Micic, O. I.; Cheong, H. M.; Fu, H.; Zunger, A.; Sprague, J. R.; Mascarenhas, A.; Nozik, A. J. Size-dependent spectroscopy of InP quantum dots. *J. Phys. Chem. B* **1997**, *101* (25), 4904−4912.

(54) Li, C.; Ando, M.; Enomoto, H.; Murase, N. Highly Luminescent Water-Soluble InP/ZnS Nanocrystals Prepared via Reactive Phase Transfer and Photochemical Processing. *J. Phys. Chem. C* **2008**, *112* (51), 20190−20199.

(55) Soni, U.; Pal, A.; Singh, S.; Mittal, M.; Yadav, S.; Elangovan, R.; Sapra, S. Simultaneous Type-I/Type-II Emission from CdSe/CdS/ZnSe Nano-Heterostructures. *ACS Nano* **2014**, *8* (1), 113−123.

(56) Groeneveld, E.; Witteman, L.; Lefferts, M.; Ke, X.; Bals, S.; Van Tendeloo, G.; de Mello Donega, C. Tailoring ZnSe-CdSe Colloidal Quantum Dots via Cation Exchange: From Core/Shell to Alloy Nanocrystals. *ACS Nano* **2013**, *7* (9), 7913−7930.

(57) Carion, O.; Mahler, B.; Pons, T.; Dubertret, B. Synthesis, encapsulation, purification and coupling of single quantum dots in phospholipid micelles for their use in cellular and in vivo imaging. *Nat. Protoc.* **2007**, *2* (10), 2383−2390.

(58) Saeboe, A. M.; Kays, J. C.; Dennis, A. M., Encapsulating Quantum Dots in Lipid-PEG Micelles and Subsequent Copper-Free Click Chemistry Bioconjugation. In *Quantum Dots: Applications in Biology*, Fontes, A., Santos, B. S., Eds.; Springer: New York, 2020; pp 95−108.